Deep Vein Thrombosis Segmentation Using Deep Learning for Volume Reconstruction from 3D Freehand Ultrasound Images

Moh Nur Shodiq[1]   **Eko Mulyanto Yuniarno[1,2]**   **Tri Arief Sardjono[3]**   **Johanes Nugroho[4]**
I Ketut Eddy Purnama[1,2*]

[1]Department of Electrical Engineering, Institut Teknologi Sepuluh Nopember, Surabaya, Indonesia
[2]Department of Computer Engineering, Institut Teknologi Sepuluh Nopember, Surabaya, Indonesia
[3]Department of Biomedical Engineering, Institut Teknologi Sepuluh Nopember, Surabaya, Indonesia
[4]Department of Cardiology, Universitas Airlangga, Surabaya, Indonesia
* Corresponding author's Email: ketut@te.its.ac.id

Abstract: Deep vein thrombosis (DVT) refers to the formation of abnormal blood clots within the inner vascular veins, typically in the legs, posing significant health risks. Traditional treatment involves suctioning the clot, monitored by X-ray angiography, which exposes patients and medical staff to radiation. This study aims to enhance DVT diagnosis and treatment by developing a 3D reconstruction method using B-mode ultrasound, linear 3D interpolation, and a multi-denoising filter approach for improved image segmentation. The research methodology includes ultrasound data acquisition with a B-mode scanner and optical tracking system, followed by 3D volume reconstruction through bin-filling and hole-filling processes. Deep learning techniques are employed to segment the blood clot in ultrasound images, and the thrombus volume is estimated. Experiments were conducted in two scenarios: 3D reconstruction using a 2D ultrasound dataset from a DVT patient and thrombus area determination using artificial datasets with fat-injected balloon phantoms. Results demonstrate the proposed method achieved an accuracy of 0.824, a specificity of 0.583, and a sensitivity of 0.955. Thrombus volume estimation yielded a mean absolute percentage error (MAPE) of 27.5%. The findings indicate that the novel method is eligible to be an alternative to reconstruct thrombus volume and accurately identifies thrombus areas in ultrasound images, offering a safer alternative to traditional X-ray-based methods.

Keywords: Segmentation, Deep learning, Volume reconstruction, Deep vein thrombosis, Ultrasound image.

1. Introduction

Deep vein thrombosis (DVT) refers to the occurrence of abnormal blood clots in the inner vascular veins. DVT generally occurs in the legs [1]. This condition can lead to amputation of the leg, even potentially life-threatening [1, 2]. Among the risk factors for DVT are advanced age (over 60 years), pregnancy, obesity, recent surgery, and cancer [1, 3, 4]. Research indicates that the annual incidence of deep vein thrombosis (DVT) cases in the United States is approximately 900,000 individuals [4]. This implies that patients with symptoms of DVT are estimated to be around 1 per 1000 of the population [1, 3, 5].

DVT is a serious, yet preventable disease. Proper diagnosis and early treatment could reduce the morbidity and potential adverse effects [1, 2]. Currently, the standard treatment procedure is to suction the blood clot using a suction machine or manual suction. This process is referred to as aspiration. It offers excellent speed, effectiveness, and performance-to-price ratio. It employs a flexible aspiration catheter that is inserted into the blood vessel to open the blocked vessel. The process of aspiration is monitored by the use of X-ray angiography. Unfortunately, this process has radiation effects on both the patient and the medics. This calls for the use of other safer modalities, such as the use of freehand ultrasound.

To date, initial screening of Deep Vein Thrombosis patients generally uses ultrasound examination [6], and DVT screening is even used in children [7]. The limitation of employing freehand ultrasound is that the outcomes are presented as 2D images. Meanwhile, 3D ultrasound data is required to quantify DVT volume. Therefore, this study aims to reconstruct DVT volume from 2D ultrasound (US) images. The 3D US reconstruction consists of a 2D ultrasound probe, an optical tracking system, and a PC-based ultrasound system. During the procedure, the ultrasound probe is held freely by hand. The reconstruction of 3D data includes two phases: bin filling and hole filling. Following the acquisition of 3D data, segmentation is implemented to identify the thrombus region.

Previous research on DVT volume reconstruction from 2D US were conducted by Puentes et al. [8]. This research proposed an approach to reconstruct thrombus volume based on ultrasound images using a linear transducer and tracker sensors with electromagnetic signals. However, location scanning by electromagnetic tracking frequently suffers from interference caused by surrounding metal or electrical devices, and the device's range of efficacy is restricted. Furthermore, the research model employed classical segmentation techniques, like deformable contours [8]. Other research, Zhao et al. proposed thrombus reconstruction using the tracking system that utilizes electromagnetic signals [9] and mechanical 3D ultrasound technology [10]. The thrombus segmentation procedure employed manual segmentation. The limitation of manual segmentation results in subjective values, as outcomes vary among operators and lack consistency.

The segmentation process is carried out aeqafter the data is obtained from the reconstruction process. An example of the use of the segmentation technique method is based on deep learning. Deep learning-based automatic segmentation has found extensive application in the field of medical image segmentation, particularly in ultrasound images. Several previous researchers have employed deep learning frameworks, including U-net [11], VGG16 [12], Resnet [13], and Inception [14]. Ultrasound images are often plagued by speckle artifacts, noise, and inadequate image quality, which can affect the accuracy of segmentation. In order to address these issues, denoising filters are commonly applied to reduce speckle noise [15, 16]. However, these filters can introduce additional challenges, such as loss of fine details, over-smoothing, and reduce contrast, potentially leading to the degradation of critical diagnostic information within image. Therefore, a more effective approach is required to reduce speckle noise while preserving important image features for accurate segmentation.

Several researchers have employed segmentation to identify DVT from ultrasound images, including using clustering techniques [17]. Nonetheless, the researchers did not show clustering results that demonstrated successful segmentation. Other researchers have studied DVT segmentation using an elliptical approach. [18]. Unfortunately, using an ellipse to determine the contour of DVT is very difficult because of the obstruction of blood vessels. Meanwhile, other researchers performed DVT segmentation and classification based on ultrasound images using a convolutional neural network (CNN) [19, 20] and deep learning techniques [15, 16] for DVT detection [21] and prediction [22]. All of these studies employed two-dimensional ultrasound images. The drawback of using 2D ultrasound images is the difficulty in determining the volume of the blood clot.

In response to the limitations and weaknesses of previous studies, this study aims to develop a 3D ultrasound system for thrombus detection by determining the thrombus volume and area based on freehand ultrasound segmentation. The first phase is 3D ultrasound reconstruction using a 3D linear interpolation approach. Then, the volume of thrombus in the 3D ultrasound is determined from the segmentation stage based on deep learning method. Afterwards, to enhance the ultrasound image, we proposed a multi-enhanced method.

This study integrates several key innovations. First, we develop a 3D reconstruction that utilizes a freehand ultrasound imaging system in combination with an optical tracking system. Second, we introduce a unique linear 3D interpolation method to minimize artifacts that arise during freehand ultrasound scanning. This technique leverages the voxel nearest neighbor algorithm to correct for missing or incomplete voxel data, thus improving the accuracy of 3D volume reconstruction. Finally, to enhance the quality of ultrasound images and improve segmentation accuracy, we propose a multi-denoising filter approach. This method combines multiple filters, including non-local means and total variation, to reduce speckle noise while preserving important image details. The resulting enhanced images are then processed using deep learning-based segmentation models such as U-Net, VGG16, Resnet, and Inception enabling more accurate and consistent segmentation results. Two datasets are employed to evaluate the performance of this system. The first dataset used a 2D ultrasound from a DVT patient, whereas the second dataset used artificial datasets with fat-injected balloon phantoms.

Our main contributions to this work include:

- Developing 3D reconstruction for deep vein thrombosis using a freehand ultrasound imaging system and optical tracking system.
- Proposing a unique approach to the linear 3D interpolation method to minimize artifacts during volume reconstruction caused by freehand ultrasound scanning based on the voxel nearest neighbor algorithm.
- Optimizing deep learning-based ultrasound image segmentation results with a novel multi-denoising filter to improve segmentation accuracy while preserving fine details.

The paper is structured in the following sections: Section 2 presents a description of the materials used and the research methodologies. Section 3 covers the experiment's results and discussion. Finally, the conclusions and further work are presented in Section 4.

2. Materials and research method

In this study, automatic diagnosis of deep vein thrombosis based on freehand ultrasound segmentation is conducted through several processes. Those processes consist of scanning using freehand ultrasound equipped with an optical tracking sensor, reconstructing volume data from 2D serial images, segmenting blood vessels and blood clots that appear in the ultrasound image, calculating the volume of blood clots, and rendering the volume for 3D visualization. Afterward, the performance testing is conducted on the 3D reconstruction, segmentation, and volume estimation models. Fig. 1 illustrates the block diagram of the proposed technique and processing procedures, including 3D volume reconstruction, image segmentation, thrombus detection, and volume rendering.

2.1. System setup

The ultrasound image data acquisition device consists of a 2D ultrasound scanner (Telemed SmartUS EXT-1M with Probe Linear L15-7L40H-5) and an optical tracking system (Optitrack V:120 trio).

For the reconstruction, we used Python 3. As for the segmentation, we employed the Adam optimizer with a learning rate (lr) of 1e-3. The loss function used was binary_cross entropy, and the evaluation metric used was mean IoU. The model was trained for 50 epochs, with early stopping implemented using a patience of 2 and monitoring the validation loss. The experiment was then run on a desktop computer with specifications: Intel i7-10700F (2.9 GHz), 32GB RAM, RTX 3080 GPU, and 1TB NVMe storage.

2.2. Dataset

In this research, there are two datasets for the development and validation of the proposed 3D reconstruction and segmentation method for DVT detection. The first dataset, referred to as the clinical DVT dataset, comprises ultrasound images collected from a clinical setting. The dataset includes 317 frames extracted from 2D freehand ultrasound videos of four patients diagnosed with DVT. Image dimensions are 432 pixels in width and 576 pixels in height. These ultrasound images were manually annotated by medical professionals to provide ground truth labels for thrombus segmentation [15]. The second dataset, known as the artificial phantom dataset, was constructed using a set of fat-filled balloon phantoms submerged in water, designed to simulate the physical properties of thrombus tissue within human veins. The dataset is in the form of 3D ultrasound. We created 4 datasets using the approach created by F. Cenni et. al [23]. We opted for fat because it closely resembles the characteristics of a thrombus. This artificial dataset consists of 394 slices extracted from four 3D datasets of fat-filled balloon phantoms. The dimensions of the images are contingent upon the 3D reconstruction. An example of the dimensions of an ultrasound image is 594 pixels in width and 569 pixels in height. The dataset used for testing the volume reconstruction capabilities of the proposed method. To enhance the generalizability of the model, data augmentation techniques, including rotation, were employed. These steps were particularly important given the relatively small size of the dataset. More details of the datasets used can be seen in Table 1.

The datasets were split into training and testing sets with an 80:20 ratio. The training set was used to train the deep learning models, while the testing set was utilized to evaluate the performance of the proposed framework. The effectiveness of the proposed segmentation method was assessed using standard metrics such as the Dice Similarity Coefficient (DSC), Hausdorff distance (HD), and the Mean Absolute Percentage Error (MAPE) for thrombus volume estimation.

Table 1. Dataset

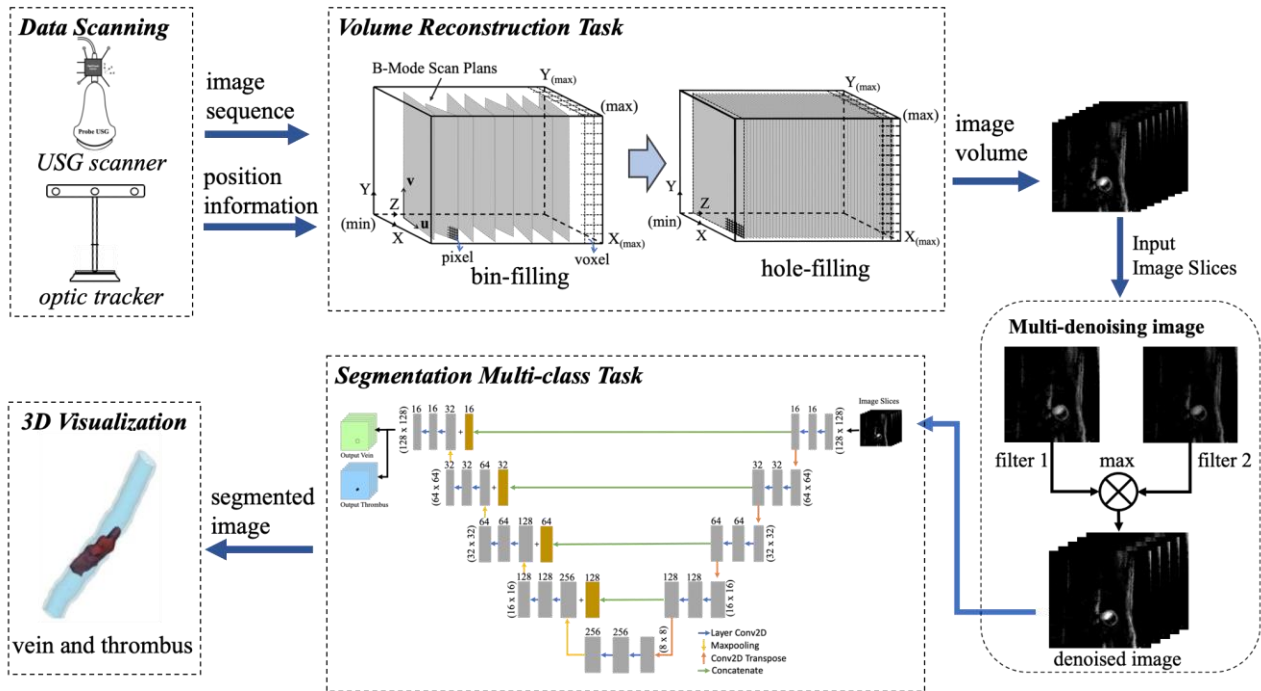| Dataset	Data	Source
Dataset 1	317 frames	Four patients with DVT symptoms
Dataset 2	Four 3D datasets; 394 slices	Artificial dataset used water and fat-filled balloons

Figure. 1 Pipeline of the proposed model for developing 3D reconstruction and automatic segmentation of deep vein thrombosis (DVT) images to determine the thrombus volume area

2.3. Volume reconstruction

After obtaining the 2D ultrasound scan image and its spatial position information, the next procedure is the 3D reconstruction of the data. The process of ultrasound volume reconstruction of deep vein thrombosis consists of three main stages: grid volume reconstruction, bin-filling, and hole-filling. Grid volume reconstruction is used to determine the volume grid, which, for example, is related to the dimensions and grid spacing; the bin-filling is used for data placement in 3D space; and the hole-filling serves to fill the gaps between images based on neighboring points.
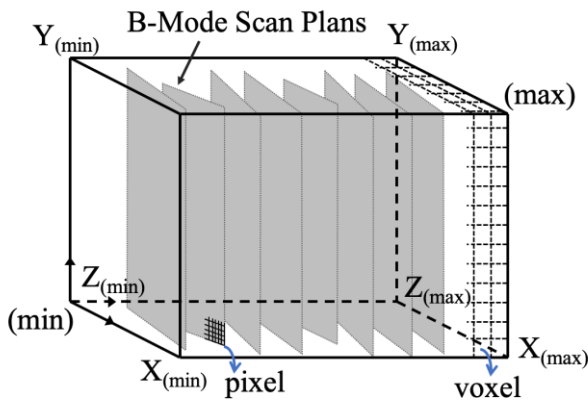

Figure. 2 Visualization of grid volume reconstruction to position the 2D ultrasound frames into 3D voxel space

Before performing the reconstruction procedure, we first configure the reconstructed voxel placement coordinate system. To do this, we apply the bounding box technique to determine the coordinate configuration of the volume. The dimensions of the 3D bounding box are obtained by identifying the minimum and maximum values at the x, y, and z coordinates. The x, y, and z axes of the volume are determined by calculating the vectors from point 0 to point $X_{(min)}$, point 0 to point $Y_{(min)}$, and point 0 to point $Z_{(max)}$. The distance of the volume grid in this study is determined by the distance between pixels in the coordinate system that has been transformed into 3D volume space, as illustrated in Fig. 2.

2.3.1. Bin-filling stage

The 2D ultrasound frame pixel is mapped into the 3D volume data voxel during the bin-filling stage based on the orientation and acquisition location. [24-27].

During volume reconstruction using a freehand ultrasound 3D system, the calibration process is a mandatory step to provide a set of fiducials that can be accurately localized both in the ultrasound images and the calibration phantom model [28, 29]. The purpose of the calibration process is to find the rigid transformation from Ultrasound image coordinates to the coordinate system of the tracking sensor mounted onto the probe [30, 31].

In this study, the calibration process used a double layer of *N*-wire phantoms [28, 29]. In the phantom, two string threads were attached. The first string has a position path of a_1-c_1-b_1-d_1. The second string follows the path position a_2-c_2-b_2-d_2, which is below the first string. The *a-b* points are on the front wall of the calibration phantom, while the *b-d* points are on the back wall of the calibration phantom. In Fig. 3, the first string is symbolized by a blue dashed straight line, and the second string is symbolized by a red dashed straight line. The distance between the string points has been determined in advance, in millimeters. The calibration method in this study uses a closed-form method, as shown in Fig. 4. As for the transformation equation in the calibration process, it is shown in Eq. (1):

$$^H X = {}^H_T T \cdot {}^T_P T \cdot {}^P_U T \cdot {}^U X \qquad (1)$$

with non-singular homogeneous transformation $({}^P_U T)^{-1} = {}^U_P T$, So as to obtain the following Eq. (2):

$$^P_U T = ({}^T_P T)^{-1} \cdot ({}^H_T T)^{-1} \cdot {}^H X \qquad (2)$$

During the bin-filling process, every pixel in the 2D frame undergoes translation and rotation. The translation and rotation process refers to the transformation result of the calibration matrix. This procedure is performed to determine the corresponding voxel position in three-dimensional space. If a voxel in 3D space is found to be unfilled with data, the voxel value is filled with the corresponding pixel value from the acquired 2D frame. The process of mapping each pixel to its corresponding position in the 3D voxel space using the transformation achieved during the calibration procedure can be defined by Eq. (3):

$$V_{(x,y,z)} = {}^T_P T \cdot {}^P_U T \cdot X^T, with\ X = \begin{pmatrix} s_x u \\ s_y v \\ 0 \\ 1 \end{pmatrix} \qquad (3)$$

Where $V_{(x,y,z)}$ is the reconstructed 3D voxel space, $^T_P T$ is the transform of the marker on the ultrasound probe to the coordinate center of the optical tracking system, $^P_U T$ is the transform of the ultrasound image plane to the marker on the ultrasound probe, *u* and *v* are the indices of in the 2D pixel image, s_x and s_y scaling factors from the pixel to millimeter ratio.

Fig. 5 (a) is an example of a single slice of a 3D ultrasound volume that was cut from the bin-filling process. In the image, there is missing data, which occurs due to the data capture and reconstruction process. The missing data is illustrated in black for ease of visual recognition, while in the data matrix, the missing data is symbolized with a value of *-1*. Data manipulation to fill the missing data in this study employs three approaches: inverse distance weighted, improved Olympic hole-filling, and linear 3D interpolation. Next, Fig. 5(b) and (c) are examples of slice images from 3D ultrasound, which are hole filled slices and mask hole filled slices, respectively.
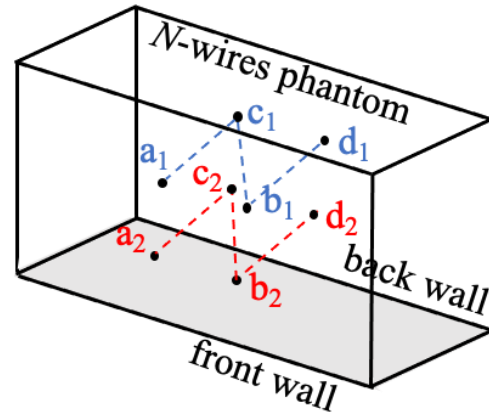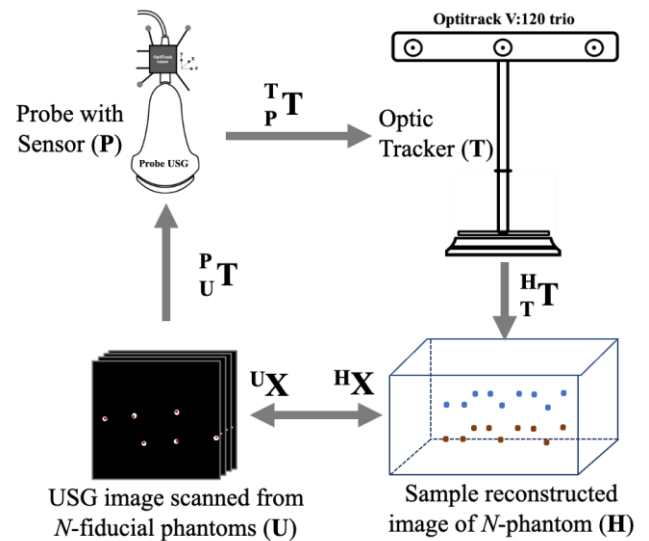

Figure. 3 Design of double N-wire phantom

Figure. 4 The procedure chart of calibration with double N-wire phantom using closed-form method

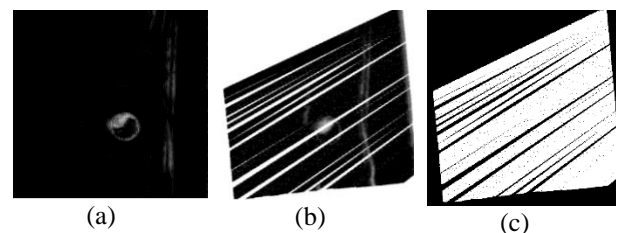(a)   (b)   (c)

Figure. 5 Example of hole filling procedure on a slice: (a) a sample of image slice, (b) a hole filled slice, and (c) a mask hole filled slice

2.3.2. Hole-filling stage

The hole-filling procedure is performed when a gap occurs in the volume reconstruction process after the bin filling process is performed. The objective of hole-filling is to estimate the value needed to fill the gap by considering the known nearby voxels. The main challenge in the hole-filling procedure is to identify the most suitable data for filling the vacant voxels within the 3D volume while ensuring no loss of information or the addition of noisy data [24].

The procedures for data hole filling are first to detect the position of the empty voxel as a whole. Next, it seeks matching data to obtain patches throughout the volume. Subsequently, the empty voxels are replaced with matching data patches. This process is repeated until all empty voxels are filled iteratively based on the repetition of the processing procedure [27].

In this study, we propose linear 3D interpolation to obtain the optimal value estimation for filling gaps in voxels. To assert the performance, the methods were compared based on a simulated 3D ultrasound image volume, including inverse distance weighted, and improved Olympic hole-filling.

A. Inverse distance weighted method

The Inverse Distance Weighted (IDW) is commonly used for image interpolation [32]. It is applied to the interpolation of images from different types of spatial data   [33]. It is simple for implementation and intuitive deterministic interpolation [34]. This approach provides acceptable accuracy in a reasonable amount of time [35]. The IDW uses a 3D matrix as in Eq. (4) below.

$$I_{IDW} = \sum_{i=1}^{N} w_i y_i \qquad (4)$$

$$w_i = \frac{d_i^{-2}}{\sum_{j=1}^{n} d_j^{-2}} \qquad (5)$$

$$d_i = \sqrt{(x_0 - x_h)^2 + (y_0 - y_h)^2 (z_0 - z_h)^2} \qquad (6)$$

Where y_i represents the data measured based on the value of the i-th neighboring voxel; N is the number of points; the weights w_i for each data point; d_i is the Euclidean distance to calculate the distance between the position of the hole voxel and the neighboring voxel $i=1,...n,$ where n is the number of neighbors. Whereas (x_h, y_h, z_h) is the coordinate position of the hole voxel and (x_0, y_0, z_0) is the coordinate position of the neighbouring voxel [35].

B. Improved olympic hole-filling method

The improved olympic hole filling method was proposed by Dewi et. al [24]. Improved Olympic is a hole filling technique based on the Pixel Nearest Neighbor (PNN) algorithm. The PNN algorithm is characterized by its simplicity and computational power. Improved Olympic is able to determine the vacant voxel by applying a threshold to the range width of its nearby voxels and using an average filter. The threshold is determined by removing the n% of the upper and lower values after sorting the data. Taking $n=10$% has been implemented in research. Then adjusting it to the average values based on neighboring voxels [24].

This study used the 3D nearby voxels technique to determine the new value for filling the vacant voxels. The estimation for empty voxels is obtained by the following Eq. (7):

$$x_e = \bar{x}_n - \left(\frac{R_n}{p}\right) \qquad (7)$$

Where x_e represents the estimated value to fill the empty voxels, $\bar{x}_n$ represents the average of the remaining sorted neighboring voxels, R_n represents the range width of the remaining sorted neighboring voxels, and p represents the threshold value, as in Eq. (8) below:

$$p = \begin{cases} p_1, & R_n \le k.\bar{R}_n \\ p_2, & R_n > k.\bar{R}_n \end{cases} \qquad (8)$$

Where $\bar{R}_n$ is the average of the range width among the neighboring voxels that are sorted in all existing vacant voxels, k is the threshold to classify the values, with $k=0.8$, $p_1=20$, and $p_2=2.5$ [24].

C. Linear 3D Interpolation.

A technique for estimating the missing data based on the known surrounding data is interpolation. This refers to determining the intensity or value of a missing voxel in the context of medical imaging by analyzing its neighbors. Linier 3D interpolation method estimates the value of a missing voxel by taking a weighted average of its immediate neighbors. Bicubic and tricubic interpolation techniques take gradients or intensity variations into consideration while examining a broader neighborhood surrounding the absent voxel. Although it requires more computing power, this produces estimates that are smoother and more accurate [36], [37].

Linear 3D interpolation is referred to as linear tetrahedral interpolation. Linear tetrahedral interpolation extends the principle of triangle interpolation into 3D space. The data points are scattered in three-dimensional space (x_i, y_i, z_i). The first step in this procedure is to divide the scattered point set in 3D space. Then, implement triangular

interpolation using the terms of the Bernstein-Bezier polynomial [38]:

$$p(u,v,w) = c_0 + c_1 u^3 + c_2 u^2 v + c_3 u v^2 +$$
$$c_4 v^3 + c_5 v^2 w + c_6 u w^2 + c_7 w^3 +$$
$$c_8 u w^2 + c_9 u^2 w + c_{10} uvw \qquad (9)$$

Where $u + v + w = 1$. The coefficient c_0, ..., c_{10} is the Bernstein-Bezier coefficient. The values of u, v, and w are the barycentric coordinates of triangle point.

2.4. Segmentation

This study used deep learning for segmentation. The input data is reconstructed data in the form of 3D volumes that are sliced into 2D images along the coronal plane. The accuracy of segmentation can be improved by utilizing image denoising [39]. Based on that, here we propose a new approach for enhanced ultrasound images with multi-denoising filters, as in Eq. (10). Furthermore, to test the accuracy, we compare the segmentation process either without filter or with multiple filters. Such filters include anisotropic diffusion, bilateral, gaussian, mean filter, median, non-local means, total variation, wavelet, and wiener.

$$I_{i,j} = max(X_{i,j} , Y_{i,j}) \qquad (10)$$

Where $I_{i,j}$ is the combined denoised image obtained from taking the maximum value between the two enhanced images using the X filter and Y filter. Where i, j is the x, y pixel position in the image.

The U-Net convolutional neural network (CNN) architecture is employed for the purpose of segmenting blood vessel walls and clots in ultrasound image sequences. To obtain better 2D ultrasound image segmentation results, variants of U-Net CNN are used, including U-Net, VGG16, Resnet, and Inception.

2.5 Evaluation metrics

The Dice similarity coefficient (DSC) and Hausdorff distance (HD) are two metrics used to evaluate the performance of segmenting thrombus sequence images. DSC indicates the degree of conformity between the overlap area of the ground truth and the prediction mask, which is defined as follows:

$$DSC = \frac{2(P \cap G)}{P \cup G} \qquad (11)$$

Where P is the prediction mask and G is the ground truth. On the other hand, HD indicates the matching difference of the image object based on the point, which is defined in the following equation:

$$HD(A,B) = max_{i,j}\left(hd(A_i, B) , hd(B_j, A)\right) \qquad (12)$$

where,

$$hd(A_i, B) = min_k\left(hd(A_i, B_k)\right) \qquad (13)$$

$$hd(B_j, A) = min_k\left(hd(B_j, A_k)\right) \qquad (14)$$

$hd(A,B)$ is the distance measurement between pixel A and pixel B, while $hd(B,A)$ is the distance between pixel B and pixel A [40].

Performance measurement of 3D freehand ultrasound reconstruction is checked based on neighboring points using mean absolute error (MAE) [24]. As for the accuracy of measurement of thrombus volume estimation, mean absolute percentage error (MAPE) is employed.

3. Experiment result and discussion.

3.1. Volume reconstruction performance

In this study, we experimented with volume reconstruction using our first dataset type. The first dataset comes from a patient with thrombus symptoms and is used for training and testing the reconstruction process. We randomly select one image from the 317 available images. Then, that image was duplicated into 312 images. Next, the image slice is arranged in a 3D plane sequentially to form 3D image data with a voxel size of 432 x 576 x 312. Furthermore, in each slice, noise is given as hole data or missing data. Hole manipulation is generated randomly for each slice. The hole distribution varies from the capacity of 0.1%; 0.5%; 1%; 2%; 3%; 4%; 5%; 6%; 8%; 10%; 12%; 15%; or 20% of the total number of pixels for each slice.

The data manipulation for filling the missing data uses a voxel nearest neighbor algorithm-based technique. We propose linear 3D interpolation to fill in the missing data. To test the accuracy of our proposed method, we compare it with other voxel nearest neighbor methods, namely inverse distance weighted and improved Olympic hole-filling.

The results of measuring the accuracy of data estimation for filling missing data can be seen in Fig. 6. The No Hole Filling method, where no attempt is made to reconstruct or fill the missing data. The MAE trend shows a sharp increase as the percentage of

missing data grows. For instance, with 0.1% missing data, the Mean Absolute Error (MAE) is relatively low at 0.001448. However, as the absence of data escalates to 20%, the Mean Absolute Error (MAE) significantly increases to 0.257696. This indicates that the gap between actual and anticipated values widens as missing data rises. The average MAE before implementing the hole-filling method is 75.37×10^{-3}.

The Improved Olympic Hole Filling method employs a sophisticated approach that handles outliers and utilizes neighboring data to estimate missing values. This method consistently demonstrates a low MAE rate across all percentages of missing data. For example, with 0.1% missing data, the MAE is remarkably low at 0.000202, and even with 20% missing data, the MAE remains comparatively stable at 0.032046. The trend shows that although the MAE increases as the percentage of missing data grows, the rate of increase is much slower compared to the other methods. This method provides robust performance even with larger amounts of missing data, making it highly effective for scenarios where data loss is substantial. The improved Olympic hole-filling method has an average MAE performance of 9.39×10^{-3}.

The Inverse Distance Weighted (IDW) approach computes missing values by assigning greater weight to proximate known data points. IDW performs well at low percentages of missing data, with a very low MAE of 0.00005 at 0.1% missing data. However, as the missing data increases, the MAE grows more rapidly compared to the Improved Olympic Hole Filling method. By the time 20% of data is missing, the MAE reaches 0.014684. While it performs admirably in situations where the missing data is minimal, IDW struggles to maintain accuracy when larger amounts of data are missing. Therefore, its performance degrades more quickly in the presence of substantial gaps in the data. the inverse distance weighted method has an average MAE value of 2.44×10^{-3}.

Linear 3D interpolation assumes a linear change between points in 3D space and is computationally efficient. The method shows exceptional performance when dealing with small percentages of missing data. At 0.1% missing data, it has the lowest MAE at 0.000025. However, as the percentage of missing data increases, the error rises significantly, particularly after the 8% threshold. For example, at 20% missing data, the error reaches 0.000576. While Linear 3D Interpolation is highly effective at lower levels of missing data, it loses its accuracy as the gaps in the data become larger. The method's assumption of linearity works well for small, simple missing
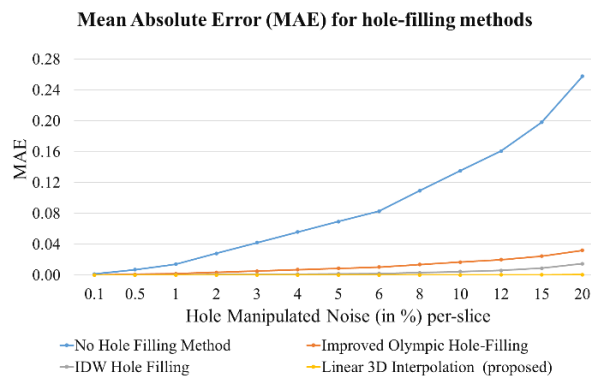

Figure. 6 Graphs of MAE measurement results for volume reconstruction performance accuracy. Orange line: by improved olympic hole-filling; gray line: by inverse distance weight; and yellow line: by 3D interpolation; while blue line: without hole-filling

regions but fails to handle complex or larger missing areas effectively. The linear 3D interpolation produces an average MAE value of 0.11×10^{-3}.

Based on the research findings, Improved Olympic Hole Filling [24] is the most balanced and effective method, performing well across different percentages of missing data. On the other hand, IDW Hole Filling [32] perform well with smaller data gaps but experience a more rapid decline in accuracy as the amount of missing data increases. Furthermore, Linear 3D Interpolation shows the best performance. It has the smallest average MAE values. Whereas, The No Hole Filling Method, has the worst performance, as it does not attempt to fill the missing data, leading to the highest MAE values overall. Accordingly, Linear 3D Interpolation is then used in the next process, which is segmentation.

3.2. Automatic segmentation performance

Automatic thrombus segmentation uses a comparison of four segmentation models namely U-net [11], VGG16 [12], Resnet [13], and Inception [14]. While denoising filters aim to enhance the quality of the image, used in this study are Wiener [41], Wavelet [42], Total Variation [43], Non Local Means [44], Median [45], Mean Filter [45], Gaussian [46], Bilateral [47], Anisotropic Diffusion [42], and combined non-local means and total variation filters (proposed method). We use dice similarity coefficient (DC) and hausdorff distance (HD) for the performance evaluation.

Based on the comparison results of thrombus segmentation performance using various denoising filters, measured by the mean Dice coefficient. Without the application of denoising filters, the segmentation performance across all deep learning architectures U-Net, VGG16, ResNet, and Inception appears suboptimal, particularly on ResNet. The use

of denoising filters such as Total Variation, Non-Local Means, and Wiener filter significantly improves the segmentation quality, particularly on U-Net and VGG16. Best performance on U-net, ResNet, and Inception with Total Variation filter achieved the performance 0.7358, 0.7014, and 0.6904 respectively. In VGG16, the Median, Non-Local Means, and Wiener filters provided notable improvements with Dice coefficients of 0.7329, 0.7390, and 0.7349, respectively. The proposed method in this study achieved the highest performance in VGG16 with a mean Dice coefficient of 0.7489, surpassing other denoising filters. The performance results as shown in Table 2.

Table 2. mean Dice Coefficient thrombus segmentation using multi denoising filter result.

	U-Net	VGG16	Resnet	Inception
No-filter	0.5909	0.6325	0.4829	0.5269
Anisotropic Diffusion	0.5677	0.7006	0.5567	0.5495
Bilateral	0.6139	0.5842	0.5489	0.6550
Gaussian	0.5787	0.5590	0.5393	0.6550
Mean Filter	0.5147	0.6867	0.5190	0.5022
Median	0.6178	0.7329	0.5529	0.5905
Non Local Means	0.6347	0.7390	0.4696	0.4755
Total Variation	0.7358	0.7125	0.7014	0.6904
Wavelet	0.4922	0.5540	0.6464	0.4300
Wiener	0.6788	0.7349	0.5547	0.5511
Proposed Method	0.6384	**0.7489**	0.4736	0.5723

Table 3. The performance of thrombus segmentation using multi denoising filter based on Hausdorff Distance

	U-Net	VGG16	Resnet	Inception
No-Filter	1.8570	1.9000	2.1319	1.9588
Anisotropic Diffusion	1.8509	1.7258	1.8790	1.9361
Bilateral	1.8827	1.8549	1.9006	1.7706
Gaussian	1.8535	1.9267	1.9619	2.0149
Mean Filter	2.0026	1.7024	1.9777	1.9668
Median	1.7849	1.6396	1.9006	1.8207
Non Local Means	1.8122	1.6335	2.0399	2.0428
Total Variation	1.8122	1.6335	2.0399	2.0428
Wavelet	1.9568	1.9006	1.8111	2.0655
Wiener	1.7745	1.6769	1.9932	1.8463
Proposed Method	1.9661	**1.6212**	2.0547	1.8822

Table 4. Thrombus Detection Results using VGG16 with multi denoising filter based on 2D ultrasound images

Predictions	Labels	
	Positive	*Negative*
Positive	42	10
Negative	2	14

Table 3 presents the performance results of thrombus segmentation. Without any denoising, the no-filter baseline shows high HD values, with ResNet having the highest at 2.1319, indicating poor performance, while U-Net achieves a slightly lower value of 1.8570. When denoising filters are applied, VGG16 consistently shows the best improvements. For example, Anisotropic Diffusion reduces the HD for VGG16 from 1.9000 to 1.7258, and Bilateral filtering lowers the HD for Inception from 1.9588 to 1.7706, demonstrating notable improvements. Among all methods, the proposed method stands out, achieving the lowest HD score of 1.6212 for VGG16, outperforming all other filters. Overall, VGG16 consistently benefits the most from denoising, particularly with the proposed method, whereas ResNet tends to show higher HD values across the board, indicating less effective performance. Inception performs well with Bilateral, while U-Net delivers strong results with Non-Local Means and Total Variation. The proposed method proves to be the most effective filter. The significant performance improvement in VGG16 indicates that this method is highly suitable for image segmentation.

The test results of the proposed thrombus detection based on VGG16 using multi denoising filter are shown in Table. 4. The test results used of 68 ultrasound image slices. The confusion matrix shows 42 true positives, 2 false negatives, 10 false positives, and 14 true negatives. The model demonstrated a sensitivity of 95.45%, meaning it accurately identified the vast majority of thrombus positive cases. However, the specificity was 58.33%, indicating a higher rate of false positives, where some non thrombus cases were incorrectly classified as positive. Despite this, the model achieved an overall accuracy of 82.35%, reflecting solid performance in correctly classifying both positive and negative cases. These results suggest the model is highly effective at detecting thrombus cases, though improvements could be made to reduce the number of false positives and improve specificity. Meanwhile, Fig. 8 shows the frequency plot based on the dice coefficient and Hausdorff distance. Fig. 9 shows an example of the segmentation results using VGG16 by applying a multi-enhanced image filter. A slice is extracted from the original ultrasound image, as illustrated in Fig. 9 (a). The image is further categorized into two

segments: the blood vessel ground truth image depicted in Fig. 9 (b), and the thrombus ground truth image illustrated in Fig. 9 (c). Meanwhile, Fig. 9 (d) illustrates the predicted blood vessel image, whereas

Figure. 8 The frequency plot value of (a) Dice Similarity Coefficient (DSC), and (b) Hausdorff distance (HD) based on thrombus segmentation results.

(a) (b) (c)

(d) (e) (f)

Figure. 9 Example of segmentation result using VGG16 by applying multi enhanced image filter: (a) original ultrasound image, (b) blood vessel groundtruth image, (c) thrombus groundtruth image, (d) and (e) predicted blood vessel and thrombus segmentation results, and (f) a comparison of predicted (red) and manual segmentation (yellow) results

Fig. 9 (e) illustrates the thrombus segmentation image. Fig. 9 (f) illustrates the comparison of predicted images (red) and the manually annotated images (yellow).
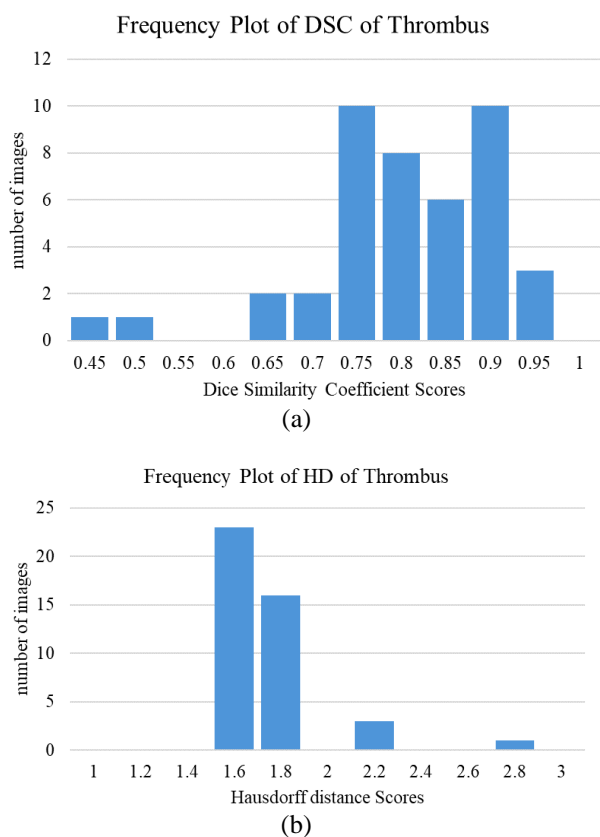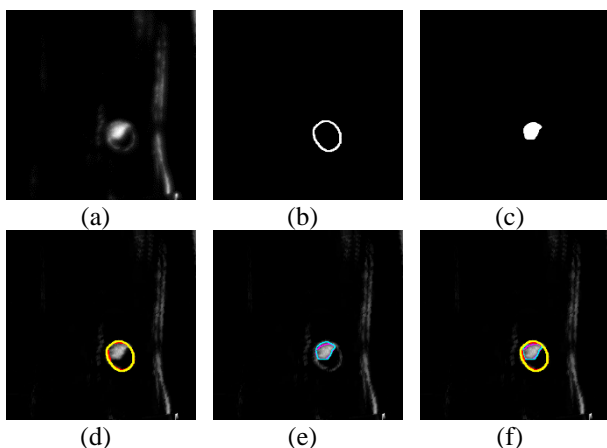
3.3. Volume thrombus estimation

Volume estimation uses the segmented thrombus contour, which is then used to calculate the volume of the thrombus clot. The thrombus volume estimation measurement uses the following equation:

$$V = \sum_{i=1}^{k}(n_i) \qquad (15)$$

where V is the total estimated thrombus volume at the longitudinal distance between the intervertebral initial layer and the final layer in pixel units, k is the total number of layers, and n_i is the number of segmented voxels in the i-th layer.

Measurement results of thrombus volume estimation from reconstructed volume data using VGG16 automatic segmentation with multi-denoising filter can be found in Table 5. The predicted result of the total volume of thrombus obtained was 43423 unit pixels. Meanwhile, the manual measurement of ground truth data is 44823 unit pixels. Based on the results of the thrombus volume estimation, the MAPE value is 27.5%. Fig. 10 illustrates the three-dimensional volume reconstructed from the segmentation of clots and blood vessels automatically. The thrombus area is represented by the inside dark red 3D volume, whereas the vessel wall area is represented by the transparent outer wall. The 3D volume visualization was rendered using 3D-slicer (www.slicer.org).

Figure. 10 Visualization of reconstructed 3D volumes from automated segmentation of blood vessels and clots. The thrombus area is represented by the inside dark red 3D volume, whereas the vessel wall area is represented by the transparent outer wall

Table 5. Measurement of thrombus volume estimation between experts vs reconstructed volume using MAPE

	Volume on ground truth (pixel)	volume estimation (pixel)	MAPE (%)
Reconstructed volume vs Expert	44823	43423	27.5

4. Conclusion

This research proposes a 3D volume reconstruction system based on freehand ultrasound segmentation. The experimental findings demonstrate the effectiveness of the proposed 3D reconstruction technique to reconstruct thrombus volume and a multi-denoising filter to enhance ultrasound images for automatic segmentation yields good results. The prediction results obtained sensitivity values of 0.955. The specificity value is 0.583. While the accuracy value is 0.824. Furthermore, the thrombus volume estimation gets a MAPE value of 27.5%. In further research, the research will focus on automatic analysis and volume rendering of deep vein thrombosis.

Notation list:

Symbol	Description
$^H X$	Location of the cable phantom within the coordinate system
$^H_T T$	Transformation matrix from optical tracking system center to cable phantom center coordinate system.
$^T_P T$	Transformation matrix from cable phantom center to optical tracker center.
$^P_U T$	Transform matrix for image pixels to probe coordinates.
$^U X$	Pixel positions on B-mode ultrasound images.
X^T	Transpose X
s_x, s_y	Comparison of pixel scale to x or y axis measurements.
u, v	Spatial coordinate position in 2D image
I_{IDW}	Inverse distance weighted
w_i	Weight values assigned to each data point.
d_i	Euclidean distance
x, y, z	Position on a three-dimensional voxel coordinate system
x_h, y_h, z_h	Coordinate location of the hole voxel
x_0, y_0, z_0	Coordinate location of the neighbouring voxel
$V_{(x,y,z)}$	The reconstructed 3D voxel space
x_e	The estimated value to fill the empty voxels
$\bar{x}_n$	Average of the remaining sorted neighboring voxels
R_n	Range width of the remaining sorted neighboring voxels
p	Threshold value
k	Threshold to classify the value
u, v, w	the barycentric coordinates
c_i	Bernstein-Bezier coefficient
$P_{(x,y,z)}$	Coordinates point (x,y,z)
$p_{(u,v,w)}$	Bernstein-Bezier polynomial
$I_{i,j}$	Combined denoised image
DSC	Dice similarity coefficient
HD	Hausdorff distance
hd	The distance between two points on a pixel grid
P	Prediction image
G	Ground truth image
V	Thrombus volume estimated

Conflicts of Interest

The authors declare no conflict of interest.

Author Contributions

Conceptualization, methodology, experiment, and manuscript, Moh Nur Shodiq; methodology, software, data visualization, Eko Mulyanto Yuniarno; formal analysis and writing—original draft preparation, Tri Arief Sardjono; data interpretation, data validation, Johanes Nugroho; supervision, writing—review and validation, I Ketut Eddy Purnama. The final manuscript was read and approved by all the authors.

Acknowledgments

References

[1] S. M. Waheed, P. Kudaravalli, and D. T. Hotwagner, "Deep Vein Thrombosis", https://www.ncbi.nlm.nih.gov/books/NBK507708/.

[2] A. C. L. Albricker *et al.*, "Joint guideline on venous thromboembolism - 2022", *Arq. Bras. Cardiol.*, Vol. 118, No. 4, pp. 797–857, 2022.

[3] M. G. Beckman, W. C. Hooper, S. E. Critchley, and T. L. Ortel, "Venous Thromboembolism: A Public Health Concern", *Am. J. Prev. Med.*, Vol. 38, No. 4, Supplement, pp. S495–S501,

2010, doi: 10.1016/j.amepre.2009.12.017.

[4] I. McKerrow Johnson, J. Shatzel, S. Olson, T. Kohl, A. Hamilton, and T. G. DeLoughery, "Travel-Associated Venous Thromboembolism", *Wilderness Environ. Med.*, Vol. 33, No. 2, pp. 169–178, 2022, doi: 10.1016/j.wem.2022.02.004.

[5] J. Stone *et al.*, "Deep vein thrombosis: pathogenesis, diagnosis, and medical management", *Cardiovasc. Diagn. Ther.*, Vol. 7, No. Suppl 3, pp. S276–S284, 2017, doi: 10.21037/cdt.2017.09.01.

[6] N. H. 'Izzah bt Mat Harun, N. bt Ibrahim, N. S. bt Aziz, W. N. S. bt Wan Zakaria, and N. F. bin Nik Fuad, "Study of vessel conditions in different categories of weight for Deep Vein Thrombosis (DVT) diagnosis", In: *Proc. of 2014 IEEE Conference on Biomedical Engineering and Sciences (IECBES)*, pp. 474–478, 2014, doi: 10.1109/IECBES.2014.7047545.

[7] K. Kardaras, N. Apostolou, G. I. Lambrou, M. Sarafidis, and D. Koutsouris, "Development and Evaluation of Advanced Image Analysis Techniques for Pediatric Deep Vein Thrombosis Imaging Scans", In: *Proc. of 2019 IEEE 19th International Conference on Bioinformatics and Bioengineering (BIBE)*, pp. 296–300, 2019, doi: 10.1109/BIBE.2019.00060.

[8] J. Puentes, M. Dhibi, L. Bressollette, B. Guias, and B. Solaiman, "Computer-assisted venous thrombosis volume quantification", *IEEE Trans. Inf. Technol. Biomed.*, Vol. 13, No. 2, pp. 174–183, 2009, doi: 10.1109/TITB.2008.2007592.

[9] L. Zhao *et al.*, "Freehand 3D Ultrasound to Measure Thrombus Volume in Patients with Acute Deep-Vein Thrombosis", *J. Vasc. Ultrasound*, Vol. 38, No. 1, pp. 23–28, 2014, doi: 10.1177/154431671403800104.

[10] L. Zhao *et al.*, "Measurement of thrombus resolution using three-dimensional ultrasound assessment of deep vein thrombosis volume", *J. Vasc. Surg. Venous Lymphat. Disord.*, Vol. 2, No. 2, pp. 140–147, 2014, doi: 10.1016/j.jvsv.2013.08.009.

[11] O. Ronneberger, P. Fischer, and T. Brox, "U-NET: Convolutional Networks for Biomedical Image Segmentation", In: *Proc. of Int. Conf. Med. Image Comput. Comput. Interv.*, Vol. 9351, No. Cvd, pp. 12–20, 2015, doi: 10.1007/978-3-319-24574-4.

[12] K. Simonyan and A. Zisserman, "Very Deep Convolutional Networks for Large-Scale Image Recognition", In: *Proc. of 3rd International Conference on Learning Representations (ICLR 2015)*, pp. 1–14, 2015.

[13] K. He, X. Zhang, S. Ren, and J. Sun, "Deep Residual Learning for Image Recognition", *CoRR*, Vol. abs/1512.0, 2015, [Online]. Available: http://arxiv.org/abs/1512.03385.

[14] C. Szegedy et al., "Going deeper with convolutions", In: *Proc. of 2015 IEEE Conference on Computer Vision and Pattern Recognition (CVPR)*, Boston, MA, USA, pp. 1-9, 2015, doi: 10.1109/CVPR.2015.7298594.

[15] M. N. Shodiq, E. M. Yuniarno, J. Nugroho, and I. K. E. Purnama, "Ultrasound Image Segmentation for Deep Vein Thrombosis using Unet-CNN based on Denoising Filter", In: *Proc of 2022 IEEE International Conference on Imaging Systems and Techniques (IST)*, pp. 1–6, 2022, doi: 10.1109/IST55454.2022.9827731.

[16] A. Ramadhani, I. K. E. Purnama, E. M. Yuniarno, and J. Nugroho, "Thrombus Segmentation in Ultrasound Deep Vein Thrombosis (DVT) Images using VGG16 and UNet based on Denoising Filters", In: *Proc of 2023 IEEE International Biomedical Instrumentation and Technology Conference (IBITeC)*, pp. 129–134, 2023, doi: 10.1109/IBITeC59006.2023.10390954.

[17] T. Berthomier *et al.*, "Unsupervised clustering of DVT Ultrasound Images using High Order Statistics", In: *Proc of 2018 IEEE International Conference on Bioinformatics and Biomedicine (BIBM)*, pp. 2495–2501, 2018, doi: 10.1109/BIBM.2018.8621187.

[18] J. Guerrero, S. E. Salcudean, J. A. McEwen, B. A. Masri, and S. Nicolaou, "Real-time vessel segmentation and tracking for ultrasound imaging applications", *IEEE Trans. Med. Imaging*, Vol. 26, No. 8, pp. 1079–1090, 2007, doi: 10.1109/TMI.2007.899180.

[19] B. Kainz *et al.*, "Non-invasive diagnosis of deep vein thrombosis from ultrasound imaging with machine learning", *npj Digit. Med.*, Vol. 4, No. 1, p. 137, 2021.

[20] R. Tanno *et al.*, "AutoDVT: Joint Real-Time Classification for Vein Compressibility Analysis in Deep Vein Thrombosis Ultrasound Diagnostics", in *Medical Image Computing and Computer Assisted Intervention*, pp. 905–912, 2018.

[21] K. S. Sultan and A. Abbosh, "Handheld Electromagnetic Scanner for Deep Vein Thrombosis Detection and Monitoring", *IEEE Trans. Antennas Propag.*, Vol. 72, No. 4, pp.

3210–3224, 2024, doi: 10.1109/TAP.2024.3367421.

[22] R. Sorano, K. S. Nawaz Ripon, and L. V. Magnusson, "Multi-Objective Evolutionary Optimization for Tuning Hyperparameters and Reducing Features in Prediction of Deep Vein Thrombosis", In: *Proc. of 2024 IEEE Congress on Evolutionary Computation (CEC)*, pp. 1–9, 2024, doi: 10.1109/CEC60901.2024.10612191.

[23] F. Cenni, D. Monari, S.-H. Schless, E. Aertbeliën, K. Desloovere, and H. Bruyninckx, "Efficient image based method using water-filled balloons for improving probe spatial calibration in 3D freehand ultrasonography", *Ultrasonics*, Vol. 94, pp. 124–130, 2019, doi: 10.1016/j.ultras.2018.11.009.

[24] D. E. O. Dewi, T. L. R. Mengko, I. K. E. Purnama, A. G. Veldhuizen, and M. H. F. Wilkinson, "An Improved Olympic Hole-Filling Method for Ultrasound Volume Reconstruction of Human Spine", *Int. J. E-Health Med. Commun.*, Vol. 1, No. 3, pp. 28–40, 2010, doi: 10.4018/jehmc.2010070103.

[25] T. Qiu, T. Wen, W. Qin, J. Gu, and L. Wang, "Freehand 3D ultrasound reconstruction for image-guided surgery", In: *Proc. of International Symposium on Bioelectronics and Bioinformations 2011*, pp. 147–150, 2011, doi: 10.1109/ISBB.2011.6107667.

[26] H.-B. Chen, R. Zheng, L.-Y. Qian, F.-Y. Liu, S. Song, and H.-Y. Zeng, "Improvement of 3-D Ultrasound Spine Imaging Technique Using Fast Reconstruction Algorithm", *IEEE Trans. Ultrason. Ferroelectr. Freq. Control*, Vol. 68, No. 10, pp. 3104–3113, 2021, doi: 10.1109/TUFFC.2021.3087712.

[27] W. Cong *et al.*, "Global Patch Matching (GPM) for freehand 3D ultrasound reconstruction.", *Biomed. Eng. Online*, Vol. 16, No. 1, p. 124, 2017, doi: 10.1186/s12938-017-0411-2.

[28] L. Mercier, "Review of Ultrasound Probe Calibration Techniques for 3D Ultrasound", PhD thesis. McGill University, 2004.

[29] G. Carbajal, A. Lasso, Á. Gómez, and G. Fichtinger, "Improving N-wire phantom-based freehand ultrasound calibration", *Int. J. Comput. Assist. Radiol. Surg.*, Vol. 8, No. 6, pp. 1063–1072, 2013, doi: 10.1007/s11548-013-0904-9.

[30] F. Rousseau, P. Hellier, M. M. J. Letteboer, W. J. Niessen, and C. Barillot, "Quantitative evaluation of three calibration methods for 3-D freehand ultrasound.", *IEEE Trans. Med. Imaging*, Vol. 25, No. 11, pp. 1492–1501, 2006, doi: 10.1109/TMI.2006.882134.

[31] P.-W. Hsu, R. W. Prager, A. H. Gee, and G. M. Treece, "Freehand 3D Ultrasound Calibration: A Review", *Advanced Imaging in Biology and Medicine: Technology, Software Environments, Applications*, pp. 47–84, 2009.

[32] C. Chen, N. Zhao, T. Yue, and J. Guo, "A generalization of inverse distance weighting method via kernel regression and its application to surface modeling", *Arab. J. Geosci.*, Vol. 8, No. 9, pp. 6623–6633, 2015, doi: 10.1007/s12517-014-1717-z.

[33] Z.-N. Liu, X.-Y. Yu, L.-F. Jia, Y.-S. Wang, Y.-C. Song, and H.-D. Meng, "The influence of distance weight on the inverse distance weighted method for ore-grade estimation", *Sci. Rep.*, Vol. 11, No. 1, p. 2689, 2021, doi: 10.1038/s41598-021-82227-y.

[34] Z. Li, K. Wang, H. Ma, and Y. Wu, "An Adjusted Inverse Distance Weighted Spatial Interpolation Method", In: *Proc of the 2018 3rd International Conference on Communications, Information Management and Network Security (CIMNS 2018)*, pp. 128–132, 2018, doi: 10.2991/cimns-18.2018.29.

[35] W. Maleika, "Inverse distance weighting method optimization in the process of digital terrain model creation based on data collected from a multibeam echosounder", *Appl. Geomatics*, Vol. 12, No. 4, pp. 397–407, 2020, doi: 10.1007/s12518-020-00307-6.

[36] T. M. Lehmann, C. Gonner, and K. Spitzer, "Survey: interpolation methods in medical image processing", *IEEE Trans. Med. Imaging*, Vol. 18, No. 11, pp. 1049–1075, 1999, doi: 10.1109/42.816070.

[37] D. R. Canelhas, T. Stoyanov, and A. J. Lilienthal, "A Survey of Voxel Interpolation Methods and an Evaluation of Their Impact on Volumetric Map-Based Visual Odometry", In: *Proc. of 2018 IEEE International Conference on Robotics and Automation (ICRA)*, pp. 3637–3643, 2018, doi: 10.1109/ICRA.2018.8461227.

[38] I. Amidror, "Scattered data interpolation methods for electronic imaging systems: a survey", *J. Electron. Imaging*, Vol. 11, No. 2, pp. 157–176, 2002, doi: 10.1117/1.1455013.

[39] F. Mohamed and C. Vei Siang, "A Survey on 3D Ultrasound Reconstruction Techniques", *Artif. Intell. - Appl. Med. Biol.*, 2019, doi: 10.5772/intechopen.81628.

[40] C. H. T. Yang, S. H. Lai, and L. W. Chang, "Reliable image matching via modified

hausdorff distance with normalized gradient consistency measure", In: *Proc of ITRE 2005 - 3rd Int. Conf. Inf. Technol. Res. Educ. - Proc.*, Vol. 2005, pp. 158–161, 2005, doi: 10.1109/ITRE.2005.1503090.

[41] B. H. S. Asli *et al.*, "Ultrasound Image Filtering and Reconstruction Using DCT/IDCT Filter Structure", *IEEE Access*, Vol. 8, pp. 141342–141357, 2020, doi: 10.1109/ACCESS.2020.3011970.

[42] S. H. Contreras Ortiz, T. Chiu, and M. D. Fox, "Ultrasound image enhancement: A review", *Biomed. Signal Process. Control*, Vol. 7, No. 5, pp. 419–428, 2012, doi: 10.1016/j.bspc.2012.02.002.

[43] S. Huang and S. Wan, "A Total Variation Denoising Method Based on Median Filter and Phase Consistency", *Sens. Imaging*, Vol. 21, No. 1, pp. 1–15, 2020, doi: 10.1007/s11220-020-00281-8.

[44] P. Coupé, P. Hellier, C. Kervrann, and C. Barillot, "Nonlocal means-based speckle filtering for ultrasound images", *IEEE Trans. Image Process.*, Vol. 18, No. 10, pp. 2221–2229, 2009, doi: 10.1109/TIP.2009.2024064.

[45] Z. Hosseini and M. H. Bibalan, "Speckle noise reduction of ultrasound images based on neighbor pixels averaging", In: *Proc of 2018 25th Iranian Conference on Biomedical Engineering and 2018 3rd International Iranian Conference on Biomedical Engineering, ICBME 2018*, 2018, pp. 1–6, doi: 10.1109/ICBME.2018.8703576.

[46] M. Wang, S. Zheng, X. Li, and X. Qin, "A new image denoising method based on Gaussian filter", In: *Proc.of 2014 Int. Conf. Inf. Sci. Electron. Electr. Eng. ISEEE 2014*, Vol. 1, pp. 163–167, 2014, doi: 10.1109/InfoSEEE.2014.6948089.

[47] C. Tomasi and R. Manduchi, "Bilateral filtering for gray and color images", In: *Proc of Sixth International Conference on Computer Vision (IEEE Cat. No.98CH36271)*, pp. 839–846, 1998, doi: 10.1109/ICCV.1998.710815.